AIAA JOURNAL
Vol. 48, No. 9, September 2010

Active Flow Control for NACA 6-Series Airfoil at $Re = 64,200$

A. Gross* and H. F. Fasel†
University of Arizona, Tucson, Arizona 85721

DOI: 10.2514/1.J050051

Earlier research for the NACA 64_3-618 airfoil has shown that lift-curve and stall behavior change noticeably when the chord Reynolds number is reduced significantly below its design value. For the same airfoil and a Reynolds number based on chord of $Re = 64,200$, separation control by pulsed vortex generator jets and a two-dimensional volume forcing that was motivated by a plasma actuator were investigated. Pulsed vortex generator jets with moderate jet velocities and the two-dimensional volume forcing were found to introduce coherent spanwise structures that are highly effective for separation control. A linear stability analysis of the time-averaged flow showed that spanwise disturbances are amplified by an instability mechanism, which explains why both control strategies are highly efficient. Angled pulsed vortex generator jets with large jet velocities were found to introduce streamwise vortices and to result in earlier transition. Although the control is highly effective, it is not very efficient, as streamwise vortices are not supported by the flow.

Nomenclature

A	=	amplitude
B	=	blowing ratio
c	=	chord length
c_d	=	drag coefficient
c_f	=	skin-friction coefficient
c_l	=	lift coefficient
c_m	=	moment coefficient
c_p	=	pressure coefficient
c_μ	=	momentum coefficient
f	=	frequency, volume force
k	=	spanwise mode number
Q	=	vortex identification criterion
r	=	radial coordinate
R	=	radius
Re	=	Reynolds number
s	=	arc length
S_{ij}	=	strain rate tensor
t	=	time
Δt	=	time interval
T	=	period
u, v	=	velocity components
u	=	wall tangential velocity
W_{ij}	=	vorticity tensor
x, y, z	=	coordinates
y	=	wall-normal coordinate
ΔZ	=	spanwise domain extent
α	=	angle of attack, complex wave number
α_r	=	wave number
α_i	=	growth rate
λ_z	=	spanwise wavelength
ρ	=	density
τ	=	duty cycle
ω_r	=	frequency
ω_x	=	streamwise vorticity
ω_z	=	spanwise vorticity

Subscripts

0	=	initial
∞	=	freestream
f	=	forcing

Presented as Paper 2009-4275 at the 39th AIAA Fluid Dynamics Conference, San Antonio, TX, 22–25 June 2009; received 7 July 2009; revision received 27 May 2010; accepted for publication 13 June 2010.

*Assistant Research Professor. Member AIAA.
†Professor. Member AIAA.

I. Introduction

FOR a large number of applications such as low-pressure turbines (LPTs), wind turbines, and unmanned aerial vehicles airfoils operate under low-Reynolds-number conditions. The low-Reynolds-number regime is usually considered to extend to chord based Reynolds numbers of up to 500,000. For such low Reynolds numbers, boundary layers can remain laminar over a large portion of the airfoil. Laminar boundary layers have a lower skin-friction drag than turbulent boundary layers. They are, however, also more prone to separate in the presence of adverse pressure gradients. Airfoils with very favorable high-Reynolds-number performance (such as highly optimized airfoils with significant laminar run and laminar drag bucket) may display poor performance at low-Reynolds-number conditions. In addition, airfoil performance at low-Reynolds-number conditions is strongly affected by factors such as freestream turbulence, surface roughness, and acoustic disturbances. In some instances, forced transition (boundary-layer trips, distributed roughness, and active flow control techniques) may be desirable to prevent laminar separation and improve performance.

This research contributes to a project in which we investigate the possibilities and limitations of scaled-flight research. When a geometrically scaled model of a full-size aircraft is built and flown, the airfoil chord Reynolds number is much smaller than for the full-size aircraft because of the smaller chord length and the lower airspeeds. Several years ago, a research project was initiated at the University of Arizona, where dynamically scaled models of general aviation aircraft such as the Aeromot 200S Super Ximango motor glider are built and flight-tested [1]. The Aeromot 200S was chosen because a full-size plane of this type is available for private use. Two 1:5-scale models for free-flight testing, and two 1:31-scale models for wind- and water-tunnel experiments were constructed. In addition, for investigating the low-Reynolds-number performance of the airfoil, two-dimensional (2-D) wing sections were built and tested in the wind and water tunnels [2,3]. Because of the large number of flight platforms and laboratory models, the Reynolds number range that can be investigated experimentally spans from a few thousands to a few millions. The overall goal of this research project is to develop the necessary technology and scientific tools to conduct scaled-flight research and to investigate the Reynolds number scalability of active flow control (AFC) techniques.

Mack et al. [2] and Heine et al. [3] carried out wind-tunnel experiments with a 2-D wing section of the Ximango airfoil, which is a NACA 64_3-618 airfoil. For $Re = 64,200$, the smallest Reynolds number that was being investigated, at low angles of attack the flow was seen to separate from the suction side near the trailing edge. As the angle of attack was progressively increased up to $\alpha = 10°$, the separation was found to move forward, resulting in a considerable loss of lift and a drag increase. For $10° < \alpha < 15°$, a laminar separation bubble established itself near the leading edge. The turbulent boundary layer downstream of this bubble reduced the amount of trailing-edge separation, resulting in a lift recovery for $10° < \alpha < 15°$. As the angle of attack was increased further, the reattached turbulent boundary layer began to separate near the trailing edge and separation moved forward. At some critical angle of attack, the trailing separation and the leading-edge bubble coalesced, resulting in an opening up of the leading-edge bubble. In the terminology of Gaster [4], a short bubble that is characterized by laminar separation, transition, and turbulent reattachment opens up or bursts, resulting in a bubble that extends over a significant portion of the geometry without reattachment (resulting in complete stall for an airfoil). The trailing-edge separation for $\alpha < 10°$ and the formation of the leading-edge separation bubble were also confirmed by coarse-grid direct numerical simulations (DNS) by Brehm et al. [5]. For achieving aerodynamic similarity between the scaled model operating under low-Reynolds-number conditions and the full-size plane, it would be desirable to recover the lift losses (model versus full size) for $\alpha < 10°$. Hain et al. [6] carried out water-tunnel experiments for the SD7003 airfoil at a chord Reynolds number of 66,000 and employed time-resolved particle image velocimetry (PIV) for visualizing the developing flow structures. At a 4 deg angle of attack, a laminar separation bubble was observed. It was found that Kelvin–Helmholtz instabilities resulted in the generation and amplification of spanwise vortices in the shear layer above the bubble, which then lead to three-dimensional (3-D) breakdown to turbulence. Jones at al. [7] employed DNS for investigating laminar separation bubbles on a NACA 0012 airfoil at $Re = 50,000$ and $\alpha = 5°$. Volume forcing upstream of the bubble was shown to promote transition to turbulence and increase aerodynamic performance. When the forcing was discontinued, the turbulence was self-sustained. Based on a series of simplified 3-D simulations, it was concluded that the naturally occurring 2-D vortex shedding makes the flow absolutely unstable to 3-D perturbations.

We investigated separation control for the NACA 64_3-618 airfoil at $Re = 64,200$. We considered pulsed vortex generator jets (VGJs) and a 2-D volume forcing that mimics a plasma actuator. Pulsed VGJs have been employed successfully in other low-Reynolds-number applications, e.g., for separation control of LPT blades [8,9]. The stunning performance of pulsed VGJs was attributed to the in-phase actuation of the jets, which introduces 2-D disturbances that are amplified by the flow (at no cost), as the result of a hydrodynamic instability [9]. Plasma actuators were also found to be highly successful for controlling separation at low-Reynolds-number conditions. Mack et al. [2] showed that separation could be reduced successfully with both turbulators (zigzag tape) and low-frequency modulated plasma generators. Rizzetta and Visbal [10] employed DNS for investigating LPT separation control by a plasma actuator. Wind-tunnel experiments for the same LPT blade geometry with steady and pulsed plasma actuator operation were carried out by Huang et al. [11,12]. It was suggested that for steady operation the flow was tripped to turbulence. The optimum reduced frequency for pulsed actuation was found to be unity. The generation of spanwise flow structures that promote mixing was identified as the dominant mechanism. Gaitonde et al. [13] employed a higher-order-accurate Navier–Stokes code and a phenomenologically derived plasma actuator model for investigating separation control for a NACA 0015 airfoil at a chord Reynolds number of 45,000. Only steady actuation was considered and the actuator location and volume-force orientation were varied. The most effective control was obtained for downstream forcing. In this case, a steady wall-jet developed that helped reduce or eliminate separation. Separation control for the same geometry with a pulsed plasma actuator was investigated by Visbal et al. [14]. Pulsed actuation was found to be more effective than steady actuation. It was concluded that transition and turbulence enhancement mechanisms are of greater importance for an effective control than the steady wall-jet momentum injection.

The remaining part of the paper is organized into three sections. In Sec. II the computational method is introduced. Section III summarizes the results of our investigations of AFC for the NACA 64_3-618 airfoil at $Re = 64,200$. Conclusions are provided in Sec. IV.

II. Computational Method

A. Governing Equations and Discretization

A research computational fluid dynamics (CFD) code that was developed in our laboratory was employed for the present investigations [15,16]. The code solves the compressible Navier–Stokes equations in the finite volume formulation. The Navier–Stokes equations are discretized with a ninth-order-accurate upwind scheme for the convective terms and a fourth-order-accurate scheme for the viscous terms. The system of equations is advanced in time with a second-order-accurate implicit Adams–Moulton scheme. The resulting system of equations is solved with a line Gauss–Seidel algorithm with Newton iteration.

B. Nondimensionalization and Coordinate Systems

Unless indicated otherwise, velocities and length scales are nondimensionalized with the freestream velocity, v_∞ and the airfoil chord c. Frequencies are nondimensionalized with v_∞/c. The x and y coordinates refer to the airfoil coordinate system. The x coordinate (abscissa) passes through the leading and trailing edges and the y coordinate (ordinate) touches the leading edge. The locally wall-normal coordinate is also referred to as y. In addition, the arc length, s, measured in clockwise direction along the airfoil surface starting from the leading edge is used. The trailing edge is located at $s/c = 1.046$, the total circumference is $s/c = 2.072$.

C. Computational Grid and Boundary Conditions

We employed a Poisson grid generator [17] for obtaining O-grids with high orthogonality and smoothness (Fig. 1). The number of cells in the circumferential and wall-normal directions were 802×200.

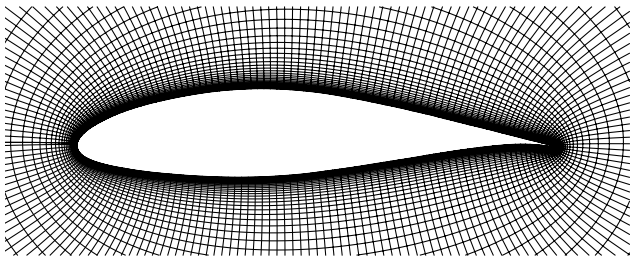

Fig. 1 Computational grid. Every fourth grid line is shown.

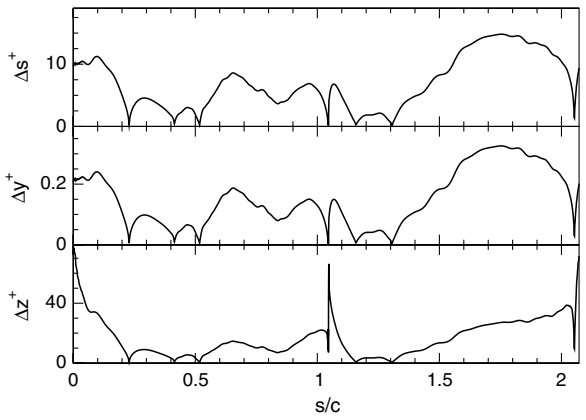

Fig. 2 Near-wall grid resolutions in wall units for uncontrolled flow.

Table 1 Suction-side near-wall grid resolutions in wall units for uncontrolled flow

	Δs^+	Δy^+	Δz^+
$s/c = 0.098$	11	0.24	33
$s/c = 0.65$	8.6	0.19	15
$s/c = 0.97$	6.9	0.15	19

The grid extent in the radial direction was more than $20c$, where c is the chord length. For the 3-D simulations, the 2-D grid was extended in the spanwise direction by $\Delta Z = 0.2c$. This domain width was chosen based on earlier LPT blade and airfoil simulations. Rizzetta and Visbal [18] performed a grid size study for a LPT blade and chose a spanwise domain width of $0.2c$. Gaitonde et al. [13] and Visbal et al. [14] employed the same domain width for their NACA 0015 airfoil simulations. The number of cells in the spanwise direction was 32. Local near-wall grid resolutions in wall units for the uncontrolled flow are shown in Fig. 2 and provided in Table 1 for three different locations (upstream of separation, $s/c = 0.098$, and in the separated-flow region, $s/c = 0.65$ and $s/c = 0.97$). As a reference, Jones et al. [7] employed grid resolutions (at the maximum skin-friction location) of $\Delta s^+ = 3.4$, $\Delta y^+ = 1$, and $\Delta z^+ = 6.5$ and Rizzetta and Visbal [10] employed grid resolutions of $\Delta s^+ = 1.13, \ldots, 47.66$, $\Delta y^+ = 0.30$, and $\Delta z^+ = 3.15$. Walls were considered to be adiabatic. For the 3-D results, periodicity conditions were enforced in the spanwise direction. A characteristics-based nonreflecting boundary condition was employed at the freestream boundary [19].

III. Results

We decided to investigate AFC for the NACA 64_3-618 airfoil at $Re = 64,200$ and for an angle of attack of $\alpha = 8.64°$. At this Reynolds number, turbulence modeling is not required and flow separation is more pronounced than for the other higher Reynolds numbers considered in the experiments [2,3]. At this particular Reynolds number and angle of attack, massive flow separation was observed in the experiments [2,3] and in earlier simulations [5]. First, the uncontrolled flow is investigated and the simulation strategy is validated through comparisons with measurements [2,3] and linear stability theory (LST). Then separation control by angled pulsed VGJs and by 2-D volume forcing that was motivated by a plasma actuator are investigated.

A. Uncontrolled Flow

We started out computing the uncontrolled natural flow for validation purposes (comparing with all available experimental data [2,3] and LST) and as a reference for later simulations with AFC. As 2-D simulations are considerably more affordable than 3-D simulations, we computed the uncontrolled flow using 2-D and 3-D simulations, to determine if some of the research could be carried out with 2-D simulations. A comparison of instantaneous flowfields (constant spanwise cross sections) is provided in Fig. 3. In the 2-D simulation, pronounced spanwise structures reside in the flow, while in the 3-D simulation, these structures quickly break up into smaller 3-D structures. Similar observations were made by Jones et al. [7] and Gaitonde et al. [13] Isocontours of the stream function for the time-averaged (and spanwise-averaged for the 3-D simulation) flowfields (Fig. 4a) show size and extent of the separated-flow region. The separation is seen to be much smaller in the 2-D simulation than in the 3-D simulation. When taking the wall pressure distribution c_p (Fig. 4b) into account, the conclusion must be drawn that the 3-D simulation data are in much better agreement with the experiment. Earlier research where we investigated separation control for a LPT blade suggests that the separation reduction in the 2-D simulation when compared with the 3-D simulation is a consequence of the overly strong spanwise coherent structures seen in the 2-D simulation [9]. Energetic spanwise coherent structures facilitate strong wall-normal mixing, which brings high-momentum freestream fluid near the wall. Both the 2-D and 3-D simulations show a

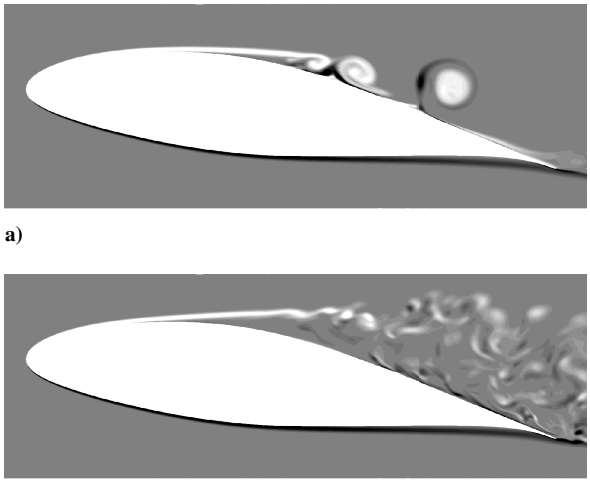

Fig. 3 Instantaneous isocontours of spanwise vorticity ($-100 < \omega_z < 100$) obtained from a) 2-D and b) 3-D simulation.

secondary separation (S'–R') in the mean skin-friction coefficient c_f (Fig. 4b). For the 2-D simulation, this secondary separation can be associated with the hump seen in the wall pressure distribution. Figure 5 provides a comparison of a clay picture from the experiment with a visualization of the wall skin-friction coefficient obtained from the 3-D simulation. (Here and in the remainder of this paper, the downstream component of the skin-friction coefficient is shown.) The clay picture indicates separation near the leading edge. The separation line is not straight and varying in the spanwise direction. In the simulation, the flow separates near 20% chord and the separation line is straight. The computed lift and drag coefficients, c_l and c_d, and earlier experimental and simulation data are shown in Fig. 6. Compared to the experimental data, lift is strongly

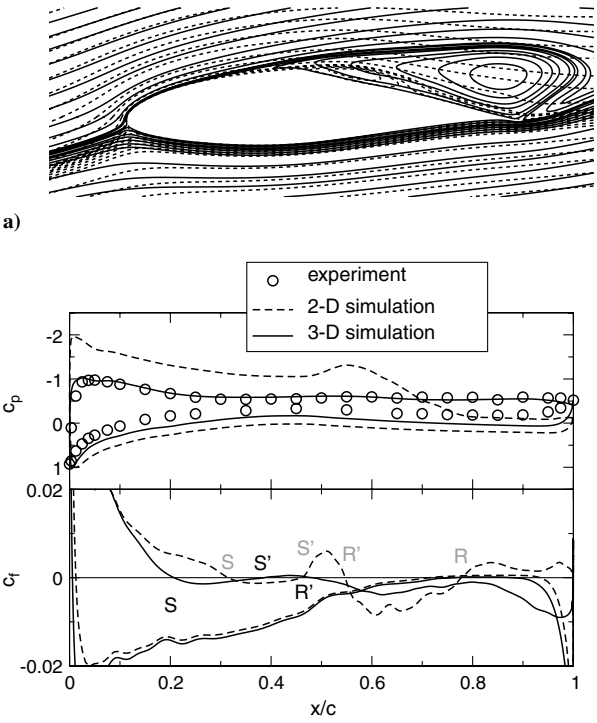

Fig. 4 Temporal and spanwise averages of 2-D (dashed lines) and 3-D (solid lines) simulations: a) isocontours of stream function and b) wall pressure and skin-friction coefficient. Experimental data by Mack et al. [2].

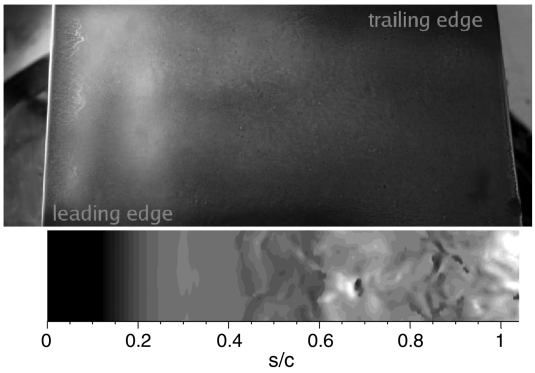

Fig. 5 Clay picture from experiments by Mack et al. [2] for $\alpha = 8.33°$ and instantaneous skin-friction coefficient ($-0.01 < c_f < 0.01$) from DNS for $\alpha = 8.64°$ (light areas indicate reverse flow).

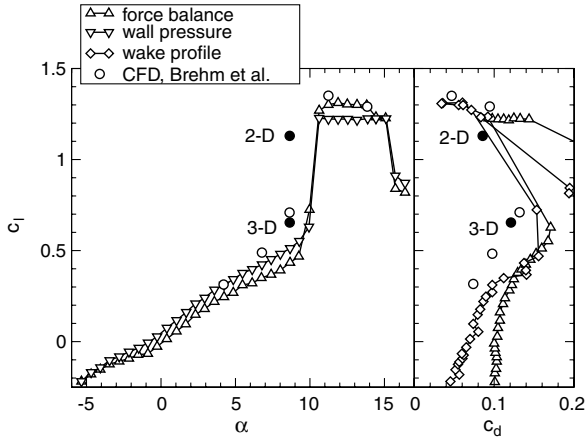

Fig. 6 Experimental lift curves and drag polars by Mack et al. [2] and earlier CFD results by Brehm et al. [5]. Present 2-D and 3-D results are indicated.

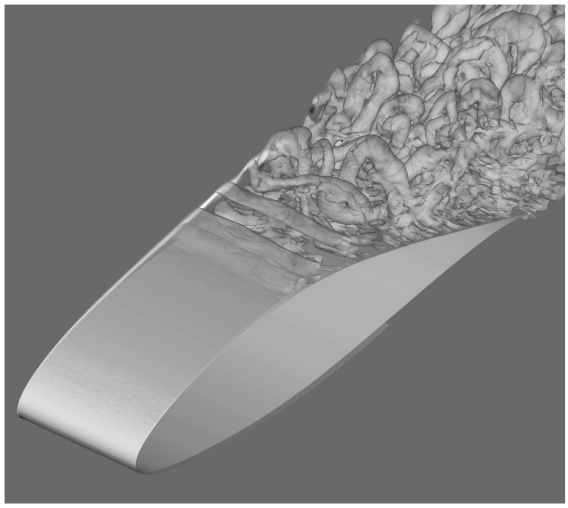

a)

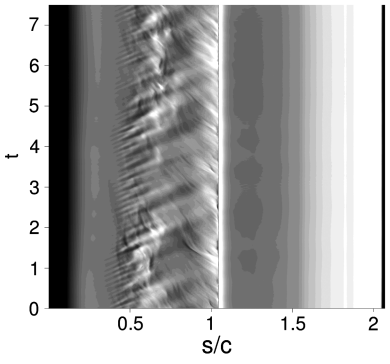

b)

Fig. 8 Images of a) instantaneous isocontours of spanwise vorticity ($-100 < \omega_z < 100$) and isosurfaces of $Q = 1$ and b) time history of spanwise average of skin-friction coefficient ($-0.01 < c_f < 0.01$).

overpredicted by the 2-D simulation. For the 3-D simulation, the predicted lift is slightly too large and the drag is slightly too low, indicating that the flow was more separated in the experiment. Time histories of the instantaneous lift and drag coefficients are shown in Fig. 7. The strong spanwise coherent structures in the 2-D simulation manifest themselves in large oscillations of the lift coefficient.

Figure 8a shows a perspective instantaneous flow visualization of the uncontrolled flow. Here, the Q vortex identification criterion [20],

$$Q = \tfrac{1}{2}(W_{ij}W_{ij} - S_{ij}S_{ij}) \tag{1}$$

was employed for visualizing vortical structures. In addition, isocontours of spanwise vorticity,

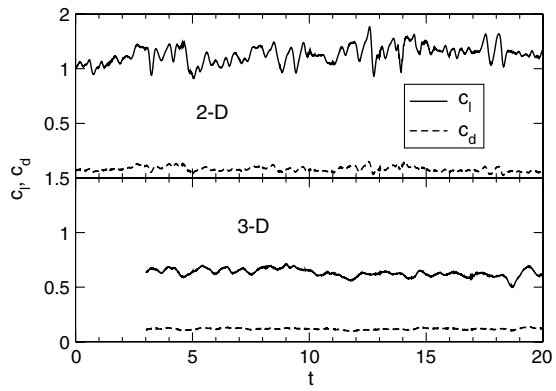

Fig. 7 Time history of lift and drag coefficients.

$$\omega_z = \frac{\partial v}{\partial x} - \frac{\partial u}{\partial y} \tag{2}$$

were included to visualize the boundary layer. As a result of a shear-layer instability (Kelvin–Helmholtz instability), the separated boundary layer rolls up into spanwise coherent structures. Similar observations were made in the experiments by Hain et al. [6], who also concluded that the primary instability was of the Kelvin–Helmholtz type. Shortly downstream of separation, the spanwise structures are modulated in the spanwise direction. This waviness, which leads to pronounced hairpin structures and later transition to turbulence, can likely be attributed to a secondary instability mechanism. In fact, airfoil simulations by Jones et al. [7] suggest that the 2-D vortex shedding makes the flow absolutely unstable to 3-D perturbations. The spanwise coherent structures modify the skin-friction coefficient. Traces of the structures can be seen in the time history of the skin-friction coefficient (Fig. 8b). Most of the traces end shortly downstream of $s/c = 0.5$, while some appear to merge and persist up to almost $s/c = 1$. Also seen are traces that originate from the trailing edge (near $s/c = 1.046$). These traces can be associated with flow structures that are transported upstream in the reverse-flow region of the separation.

The time-dependent skin-friction coefficient can be Fourier-decomposed in the spanwise direction (mode number k with spanwise wavelength $\lambda_z = 0.2/k$) and in time (frequency f), as shown in Fig. 9. Because the natural shedding is not periodic in time, the spectra are very broad, as also observed by Jones et al. [7] and Hain et al. [6] The mode $k = 0$ spectrum (Fig. 9a) shows nonzero amplitudes for $f < 10$ near $s/c = 0.5$ and a reduction of the disturbance frequencies for $s/c > 0.5$. Shortly upstream of the

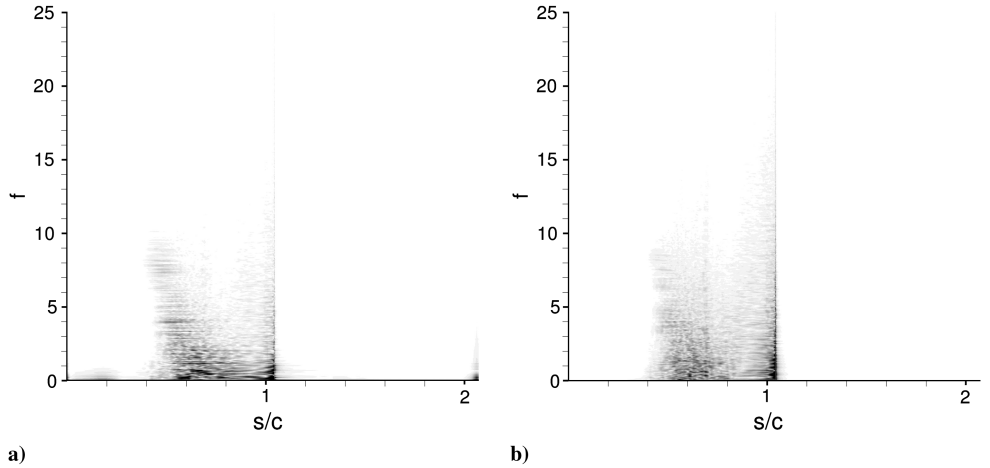

Fig. 9 Fourier transform in time of skin-friction coefficient for spanwise mode a) $k = 0$ and b) $k = 1$ ($0 < A(c_f) < 0.001$).

trailing edge, most disturbance frequencies are in the low-frequency part of the spectrum ($f < 2$). Figure 9b shows the frequency content of mode $k = 1$. The $k = 1$ spectrum clearly coincides with the $k = 0$ spectrum, indicating that the emergence of 3-D modes is linked to the presence of the 2-D mode (3-D modes can also be unstable by themselves; e.g., 3-D primary unstable modes do not need a 2-D mode to grow).

To gain additional insight into the flow physics we also carried out an LST analysis for the temporal and spanwise average of the time-dependent flow. Isocontours of the wall tangential velocity and velocity profiles at five different downstream stations for the unrolled flow are shown in Fig. 10a. Eigenvalue spectra for $f = 1$ ($\omega_r = 2\pi f = 2\pi$) and $f = 0.5$ ($\omega_r = 2\pi f = \pi$) are shown in Fig. 10b. We are interested in convective modes that are amplified and, therefore, looked at eigenmodes in the lower right quadrant. We did not consider modes with negative phase speed, ω_r/α_r. Such modes are a necessary prerequisite for the existence of an absolute instability. With our present analysis we did not attempt to determine if an absolute instability was present. We solely concentrated our attention on downstream traveling convective modes. Eigenfunctions for the unstable modes are plotted in Fig. 11a. At $s/c = 0.199$, the unstable mode is a wall mode (Tollmien–Schlichting type). For $s/c = 0.450$, the eigenfunction indicates a shear-layer mode (maximum near inflection point of velocity profile, Kelvin–Helmholtz type). For $s/c \geq 0.598$, two unstable modes are present that borrow elements from both the wall mode and the shear-layer

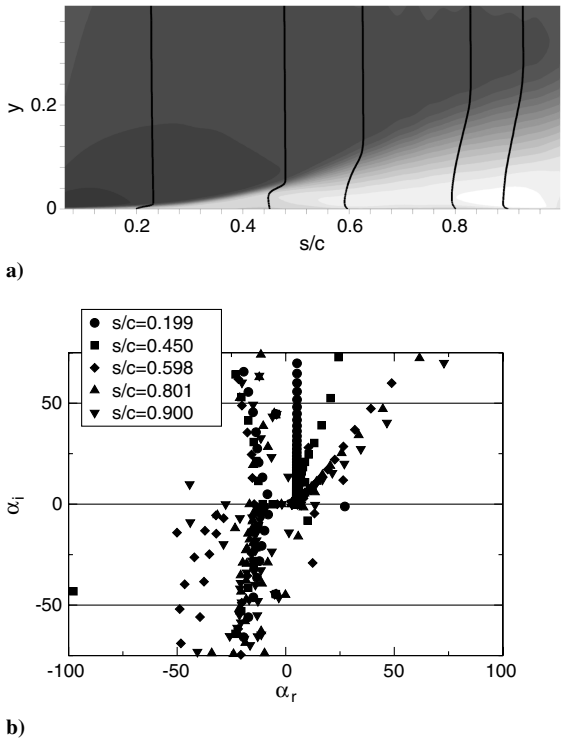

Fig. 10 Plots of a) isocontours of wall tangential velocity ($-0.3 < u < 2$) and velocity profiles at $s/c = 0.199$, 0.450, 0.598, 0.801, and 0.900 ($\Delta(s/c) = 0.025u$) and b) LST eigenvalue spectra for $f = 1$ ($s/c = 0.199$, 0.450, 0.598) and $f = 0.5$ ($s/c = 0.801$, 0.900).

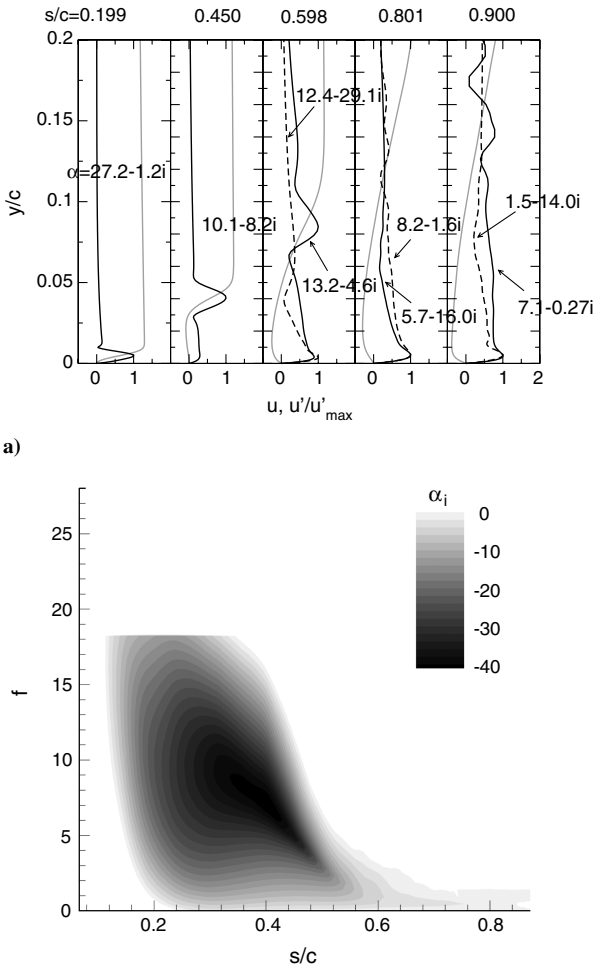

Fig. 11 Plots of a) velocity profiles (gray lines) and normalized u component of eigenfunctions and b) stability diagram.

mode. By tracking the most unstable mode, starting from $\alpha = 10.1 - 8.2i$ at $s/c = 0.450$, we generated a stability diagram (Fig. 11b). Downstream of separation ($s/c > 0.2$), disturbances are amplified for a broad range of frequencies. Further downstream for $s/c > 0.5$, as the shear layer widens, only low-frequency disturbances ($f < 2$) are amplified and the amplification rates are strongly reduced. The downstream development of several 2-D modes were compared by extracting data along lines of constant frequency from Figs. 9a and 11b. The LST mode amplitudes were obtained by integration of the growth rates:

$$A = A_0 \exp - \int_{s_0}^{s} \alpha_i(s)\, \mathrm{d}s \tag{3}$$

where A_0 can be adjusted freely since LST assumes linear behavior. We label disturbances by their frequency, f, and spanwise mode number, $k = \Delta Z/\lambda_z$, as (f, k). Figure 12 illustrates that 2-D disturbances with frequencies of $f = 1$, 5, and 10 follow the LST prediction for $s/c > 0.3$, indicating that a linear instability (based on the eigenfunction shape likely a shear-layer instability mechanism) is present. For $s/c > 0.5$, the mode amplitudes appear to level off (or saturate). Still, the disturbance amplitudes for $f = 1$ and $f = 5$ continue to follow the LST results.

B. Controlled Flow

We investigated AFC by pulsed VGJs and a 2-D volume forcing that was motivated by a plasma actuator. For the pulsed VGJ control, we employed a reduced-duty-cycle forcing, where the maximum jet exit velocity was

$$v_f(t) = \begin{cases} Bv_\infty & \text{if } 0 \le t \le \tau T \\ 0 & \text{if } \tau T < t < T \end{cases} \qquad v_f(t+T) = v_f(t) \tag{4}$$

The duty cycle τ, which is defined as the ratio of control on duration to period T, was 10%. We employed blowing ratios of $B = 1$ and 4 (ratio of maximum jet velocity to freestream velocity v_∞). The forcing frequency was $f = 5$, which corresponds to a period of $T = 1/f = 0.2$. In their NACA 0015 simulations, Visbal et al. [14] varied the forcing frequency between 1 and 8 and found 4 to be most effective. The VGJs were modeled by a wall boundary condition for the jet exit velocity with parabolic velocity distribution in the radial direction, $v = v_f[1 - (r/R)^2]$. The VGJs were located slightly upstream of the separation point at $x = 0.267c$ and had a spanwise spacing of $0.2c$. The jets were issued at a skew and pitch angle of 90 and 30°, respectively, (Fig. 13). The individual holes had dimensions of $\mathrm{d}s \times \mathrm{d}z = 0.022 \times 0.044$ and were resolved with 7×6 cells. This corresponds to a hole with diameter $\approx 0.02c$ that is drilled at an angle of 30° to the surface. The momentum coefficient,

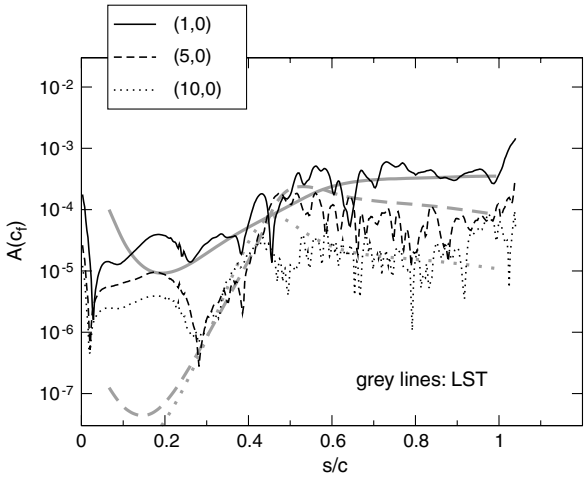

Fig. 12 Mode amplitudes obtained from DNS and LST.

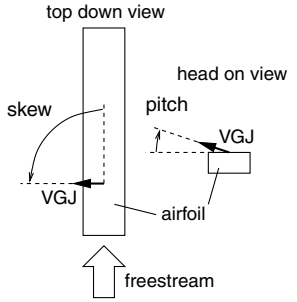

Fig. 13 Skew and pitch angle.

$$c_\mu = \frac{\iint (\frac{1}{T}\int \rho_f v_f^2 \,\mathrm{d}t)\,\mathrm{d}s\,\mathrm{d}z}{\frac{1}{2}\rho_\infty v_\infty^2 c\Delta Z} \tag{5}$$

is integrated over the jet exit hole and one forcing period T. For the subsonic cases considered here, $\rho_f = \rho_\infty$. For reduced-duty-cycle blowing through circular holes with radius R and spanwise hole spacing ΔZ, and assuming a parabolic velocity distribution over the holes, the momentum coefficient becomes

$$c_\mu = \frac{2}{3}\frac{\pi R^2}{c\Delta Z}\tau B^2 \tag{6}$$

With a cross-sectional area of

$$\pi R^2 \approx \pi/4\,\mathrm{d}s\,\mathrm{d}z \sin 30^\circ = \pi \times 0.022/2 \times 0.044/2 \times \sin 30^\circ$$
$$= 3.8 \times 10^{-4}$$

(sin 30° accounts for the fact that the holes are drilled at an angle), momentum coefficients of $c_\mu = 1.3 \times 10^{-4}$ and $c_\mu = 2.0 \times 10^{-3}$ are obtained for $B = 1$ and $B = 4$, respectively.

We also employed wall tangential volume forcing in an attempt to model a plasma actuator. The volume force was 2-D: i.e., constant across the span and with a zero spanwise component. The volume-forcing magnitude was adjusted until a velocity profile and integral force were obtained that matched PIV data and force balance measurements for a flat-plate tabletop model (not shown). For the present simulations, the volume-forcing magnitude was 7.5 (nondimensionalized by $\rho_\infty v_\infty^2/c$) and constant over the dimensions of the box indicated in Fig. 14. The downstream and wall-normal dimensions of the area in which the volume force was applied were 0.0056×0.0039. This model must be understood as a 2-D volume forcing motivated by plasma actuators and should not be confused with phenomenologically derived plasma actuator models (e.g., Rizzetta and Visbal [10], and Gaitonde et al. [13]). For the volume forcing, we also employed a reduced duty cycle with $\tau = 10\%$ and $f = 5$ [Eq. (4), with velocities and blowing ratio replaced by

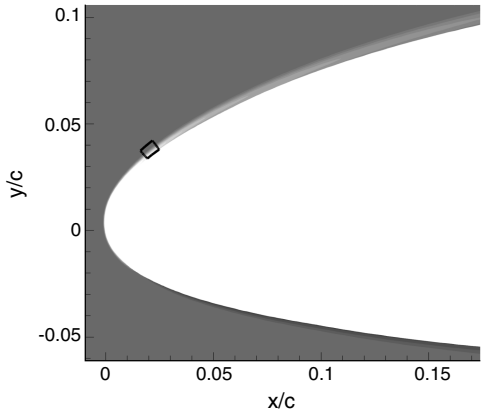

Fig. 14 Area in which volume force is applied for plasma actuator model; isocontours of spanwise vorticity; $-1000 < \omega_z < 1000$.

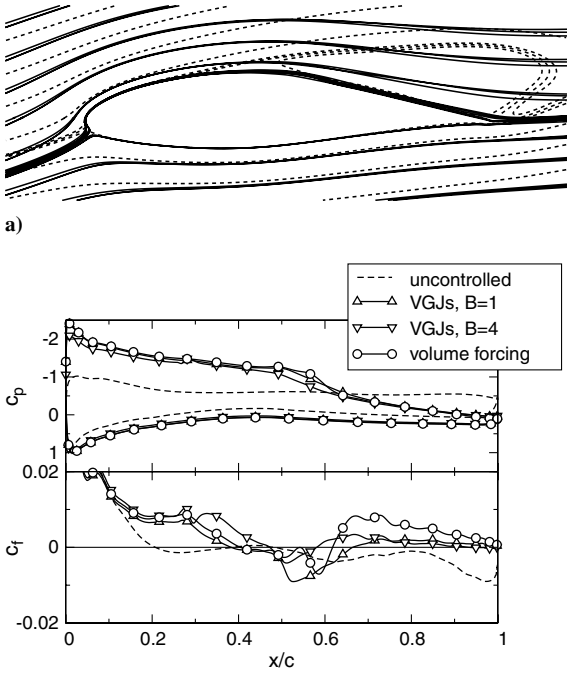

Fig. 15 Plots of a) isocontours of stream function (dashed lines: uncontrolled flow; solid lines: controlled flow) and b) wall pressure and suction-side skin-friction coefficient.

volume-forcing magnitude]. Analogously to Eq. (5), a momentum coefficient can be defined:

$$c_\mu = \frac{\int \frac{1}{T} \iiint f \,\mathrm{d}x\,\mathrm{d}y\,\mathrm{d}z\,\mathrm{d}t}{\frac{1}{2}\rho_\infty v_\infty^2 c \Delta Z} = 2\tau \times 7.5 \times (\mathrm{d}s \times \mathrm{d}n) = 3.3 \times 10^{-5} \tag{7}$$

A comparison of the stream function (for the temporal and spanwise average of the flowfield) and wall pressure and skin-friction distributions for the uncontrolled flow and the cases with flow control is given in Fig. 15. Pulsed VGJs and volume forcing appear equally effective at reducing flow separation. The suction-side separation in the back is virtually eliminated. All that remains is a small separated-flow region near the maximum-thickness location. Computed lift c_l, drag c_d, and pitching moment c_m coefficients are listed in Table 2. Also provided are the lift-to-drag ratio c_l/c_d, which is a measure of the aerodynamic efficiency, the momentum coefficient c_μ, which is a measure of the control effort, and the time-averaging intervals Δt, which were chosen to be shorter for the controlled cases, because with flow control, the shedding was more time-periodic. With flow control, the lift is increased and the drag is reduced. The highest gain in aerodynamic performance (4.9-fold increase) is obtained for the VGJs with $B = 1$ and the volume forcing. Interestingly, the volume forcing is equally effective as the pulsed VGJs with $B = 1$, despite the 3.9-times-smaller momentum coefficient, and the pulsed VGJs are more effective for the smaller momentum coefficient. Jones et al. [7] observed a gain in lift/drag of 23% for a NACA 0012 airfoil at $Re = 50,000$ and $\alpha = 5$ deg when time-periodic volume forcing

Table 2 Momentum coefficient, lift and drag coefficients, lift/drag ratio, moment coefficient, and time-averaging intervals

	c_μ	c_l	c_d	c_l/c_d	c_m	Δt
Uncontrolled, 2-D	-	1.13	0.0856	13.2	−0.112	20
Uncontrolled, 3-D	-	0.654	0.121	5.42	−0.108	17
VGJs, $B = 1$	1.3×10^{-4}	1.24	0.0465	26.6	−0.0948	9
VGJs, $B = 4$	2.0×10^{-3}	1.12	0.0485	23.1	−0.0797	3.6
Volume forcing	3.3×10^{-5}	1.26	0.0473	26.6	−0.0940	8

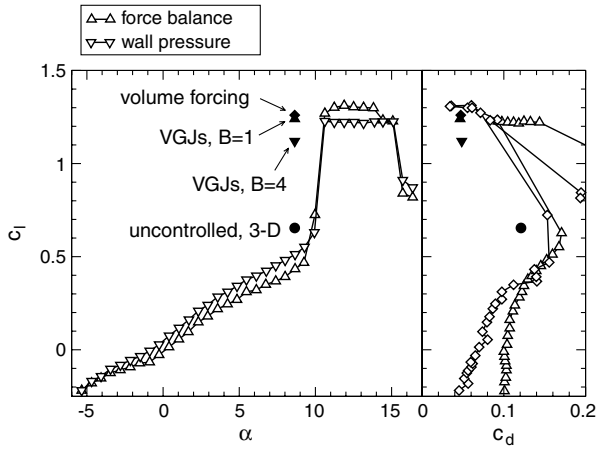

Fig. 16 Experimental lift curves and drag polars by Mack et al. [2]. Present results are indicated.

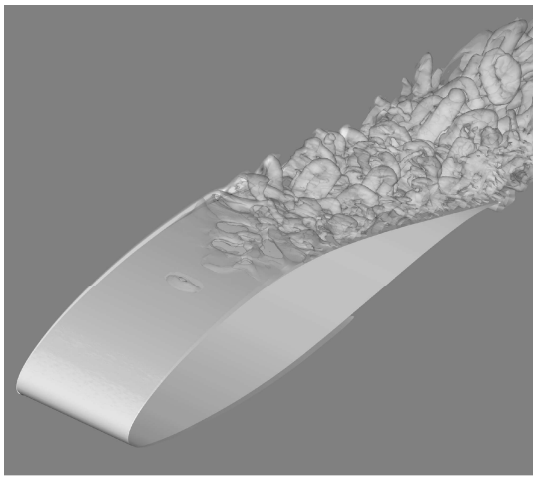

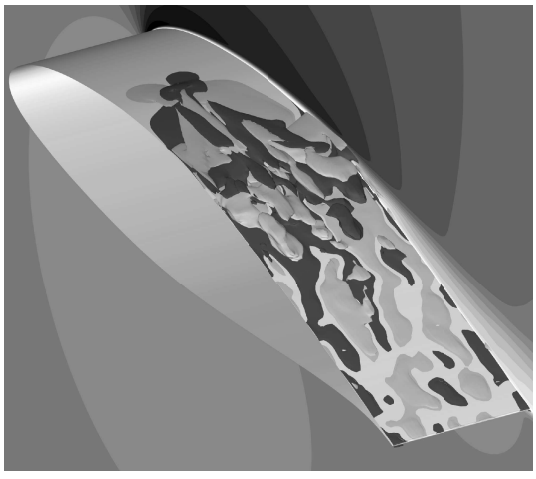

Fig. 17 Images of a) instantaneous isocontours of spanwise vorticity ($-100 < \omega_z < 100$) and isosurfaces of $Q = 1$ and b) isocontours of velocity magnitude and isosurfaces of $\omega_x = -10$, 10 for temporal average.

was applied upstream of separation. The pitching moment coefficient was computed for the quarter-chord point. With flow control, pressure is recovered in the rear part of the airfoil on the suction side (Fig. 15b), resulting in reduced pitching moments (less nose-down tendency). A graphic representation of the lift and drag data is

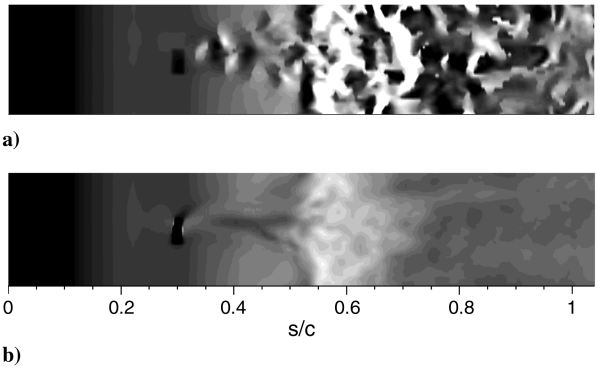

Fig. 18 Images of a) instantaneous and b) time-averaged suction-side skin-friction coefficient ($-0.01 < c_f < 0.01$).

provided in Fig. 16. With flow control, the low-Reynolds-number performance loss is recovered. In the following, we look in more detail at the flow physics associated with the different flow control approaches.

1. Pulsed Vortex Generator Jets, $B = 1$

Figure 17 shows perspective views of the instantaneous and time-averaged flow. The flow appears to transition downstream of the maximum-thickness location. No pronounced spanwise coherent structures as for the uncontrolled flow (Fig. 8a) are seen. In the time average, the isosurfaces of longitudinal vorticity,

$$\omega_x = \frac{\partial w}{\partial y} - \frac{\partial v}{\partial z} \tag{8}$$

indicate a weak streamwise vortex originating from the VGJ hole. Similar observations can be made when scrutinizing skin-friction coefficient distributions of the instantaneous and time-averaged data (Fig. 18). We also analyzed the time-dependent skin-friction coefficient. The traces seen in Fig. 19a are spaced at an interval of $\Delta t = 0.2$, which is the period of the actuation. In the frequency domain (Fig. 19b), these traces manifest themselves as lines with significant nonzero amplitudes near $f = 5$ and 10 (first higher harmonic). (The reduced-duty-cycle actuation introduces the fundamental, $f = 5$, and its higher harmonics [9].) Although spanwise coherent structures are not visible in the instantaneous flow visualization (Fig. 17a), Figs. 19a and 19b suggest that structures with considerable spanwise coherence are present.

We also employed LST for investigating local convective instability mechanisms. The time-averaged flow with a velocity profile taken in the separation bubble as well as the computed eigenvalue spectrum for that profile and $f = 5$ are shown in Fig. 20. The u' and v' components of the eigenfunction associated with the

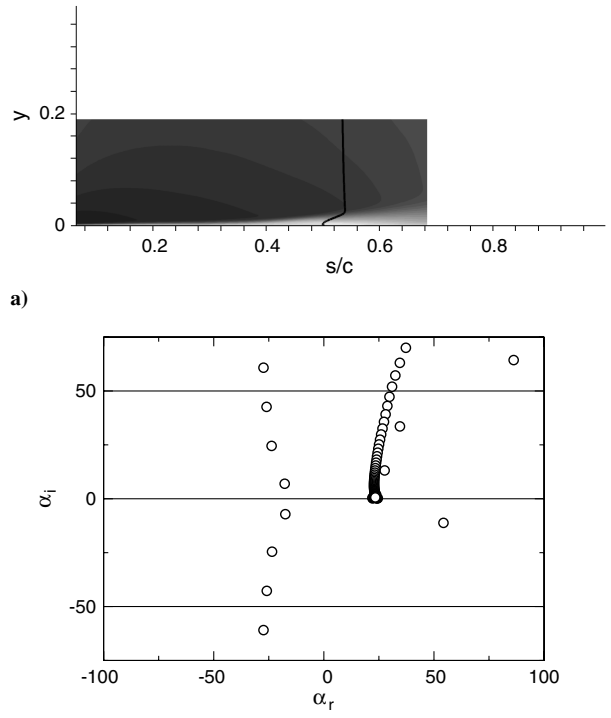

Fig. 20 Plots of a) isocontours of wall tangential velocity ($-0.3 < u < 2$) and velocity profile at $s/c = 0.503$ ($\Delta(s/c) = 0.025u$) and b) LST eigenvalue spectrum for $f = 5$ ($s/c = 0.503$).

unstable eigenvalue $\alpha = 54.3 - 11.2i$ are plotted in Fig. 21a. The complete stability diagram is shown in Fig. 21b. A viscous instability (Tollmien–Schlichting type) was identified for $x/c < 0.3$, while in the separated-flow region $0.38 < x/c < 0.66$, a mixed mode (the eigenfunction shows maxima near the wall and near the inflection point of the velocity profile) was identified. The growth rates are larger in the separated-flow region (more negative α_i). Finally, a comparison of skin-friction mode amplitudes extracted from the simulation and the LST is provided in Fig. 22. The receptivity of the flow to the actuation is low. All mode amplitudes drop by a factor of 10 or more downstream of the VGJ location, $s/c = 0.267$. Out of the multitude of modes, only the dominant modes are pointed out here. Downstream of the VGJ holes, mode (10,1) is dominant for $0.32 < s/c < 0.47$. Mode (5,0), the 2-D mode associated with the VGJ pulsation frequency, is dominant for $0.47 < s/c < 0.54$. For $0.36 < s/c < 0.5$, its amplitude follows the LST prediction, indicating that a linear instability mechanism (exponential

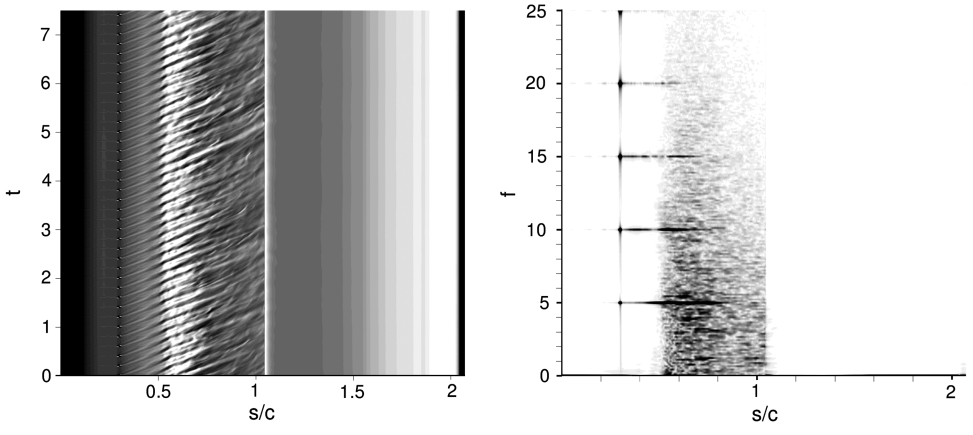

Fig. 19 Plots of a) time history of spanwise average of skin-friction coefficient ($-0.01 < c_f < 0.01$) and b) Fourier transform in time of skin-friction coefficient for spanwise mode $k = 0$ ($0 < A(c_f) < 0.001$).

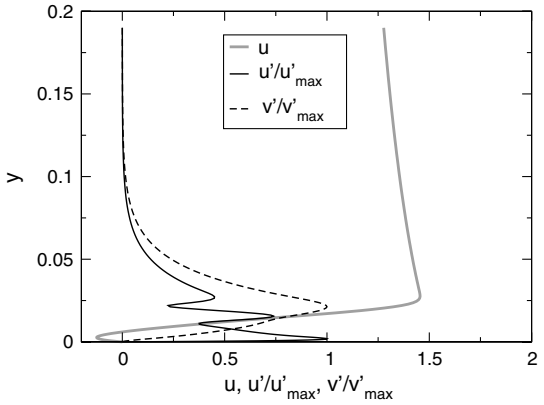

a)

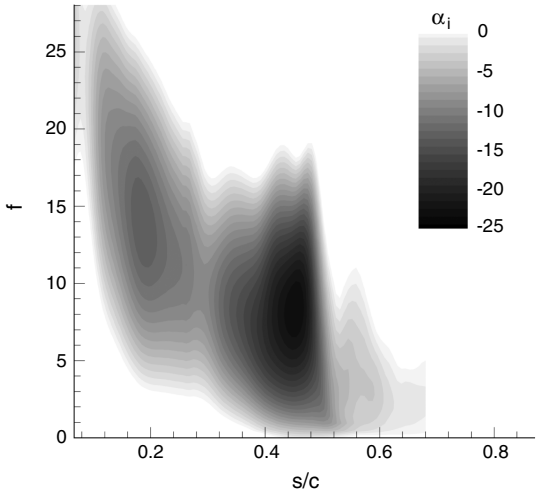

b)

Fig. 21 Plots of a) velocity profile at $s/c = 0.503$ and normalized u and v components of eigenfunction for $\alpha = 54.3 - 11.2i$ and $f = 5$ and b) stability diagram.

disturbance growth rather than transient growth) is responsible for the amplification of the disturbance input. Based on these results and our earlier research into pulsed VGJ separation control for LPT blades [9], we concluded that the presence of spanwise coherent structures (which promote wall-normal mixing and transport high-momentum freestream fluid toward the wall) and the linear amplification of these structures are responsible for the high effectiveness and efficiency of pulsed VGJs with moderate blowing ratios ($B \approx 1$ and less).

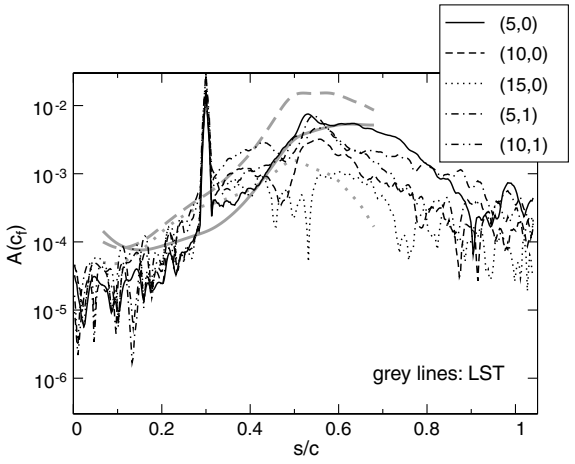

Fig. 22 Mode amplitudes obtained from DNS and LST.

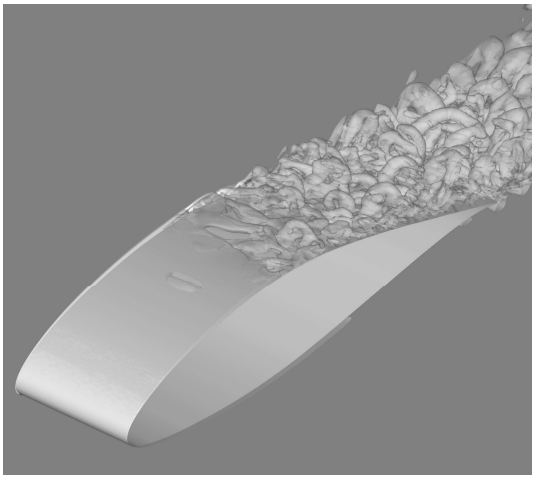

a)

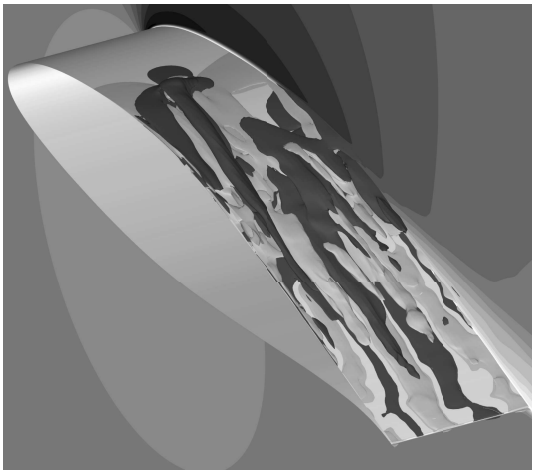

b)

Fig. 23 Images of a) instantaneous isocontours of spanwise vorticity ($-100 < \omega_z < 100$) and isosurfaces of $Q = 1$ and b) isocontours of velocity magnitude and isosurfaces of $\omega_x = -10$, 10 for temporal average.

2. *Pulsed Vortex Generator Jets, $B = 4$*

We then raised the blowing ratio to $B = 4$. The instantaneous flow visualization in Fig. 23a looks similar to the corresponding picture for $B = 1$ (Fig. 17a). However, in the time average, a longitudinal vortex that is slanted in the spanwise direction appears (Figs. 23b and 24). This observation is in agreement with PIV measurements by Hansen and Bons [21] for a flat-plate boundary layer with adverse pressure gradient. Their experiments with pulsed angled vortex

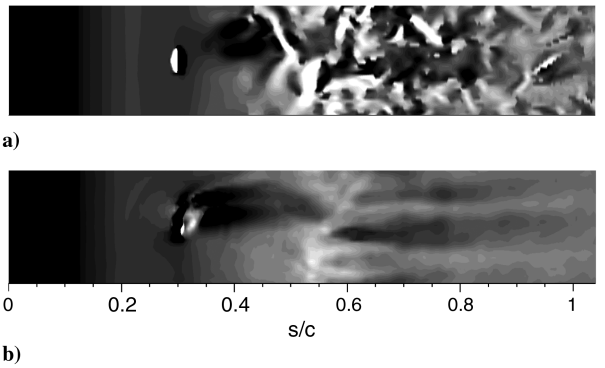

a)

b)

Fig. 24 Images of a) instantaneous and b) time-averaged suction-side skin-friction coefficient ($-0.01 < c_f < 0.01$).

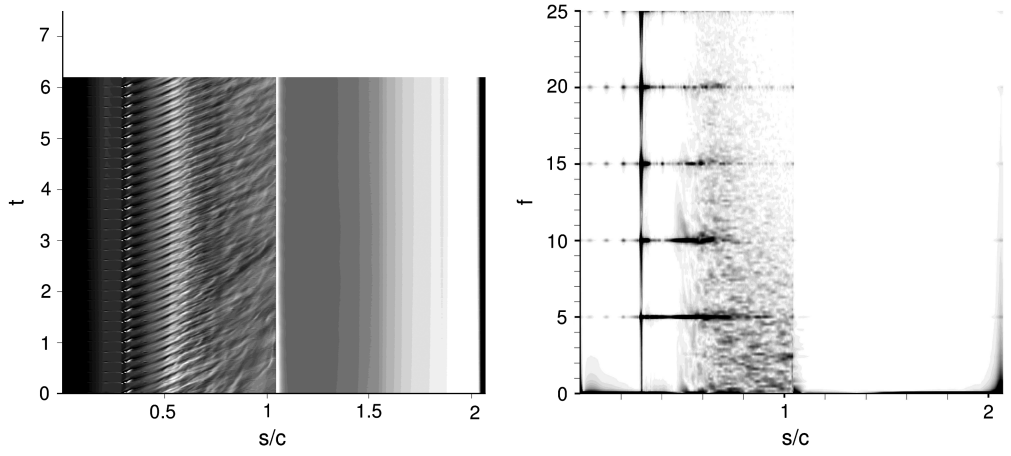

a) b)

Fig. 25 Plots of a) time history of spanwise average of skin-friction coefficient ($-0.01 < c_f < 0.01$) and b) Fourier transform in time of skin-friction coefficient for spanwise mode $k = 0$ ($0 < A(c_f) < 0.001$).

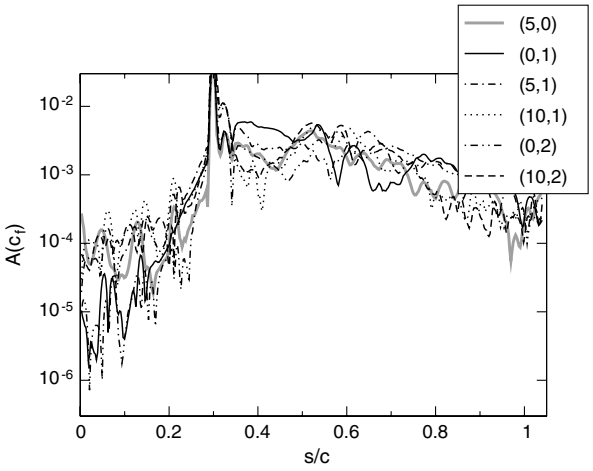

Fig. 26 Mode amplitudes obtained from DNS.

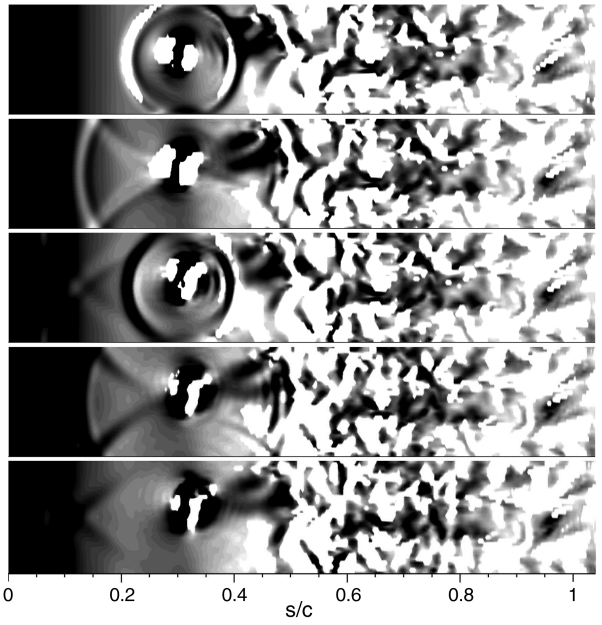

Fig. 27 Skin-friction coefficient snapshots ($0 < c_f < 0.01$, white indicates negative skin friction) for $\Delta t = 0.01$, 0.02, 0.03, 0.04, and 0.05 counting from the beginning of the duty cycle.

generator jets with $B = 3$ also indicated the presence of (in the mean) pronounced streamwise vortices.

A time–space diagram of the spanwise average of the skin-friction coefficient is shown in Fig. 25a. Near $s/c = 0.5$, the wall traces are spaced at $\Delta t = 0.2$ (the actuation period), while for $s/c > 0.6$, the

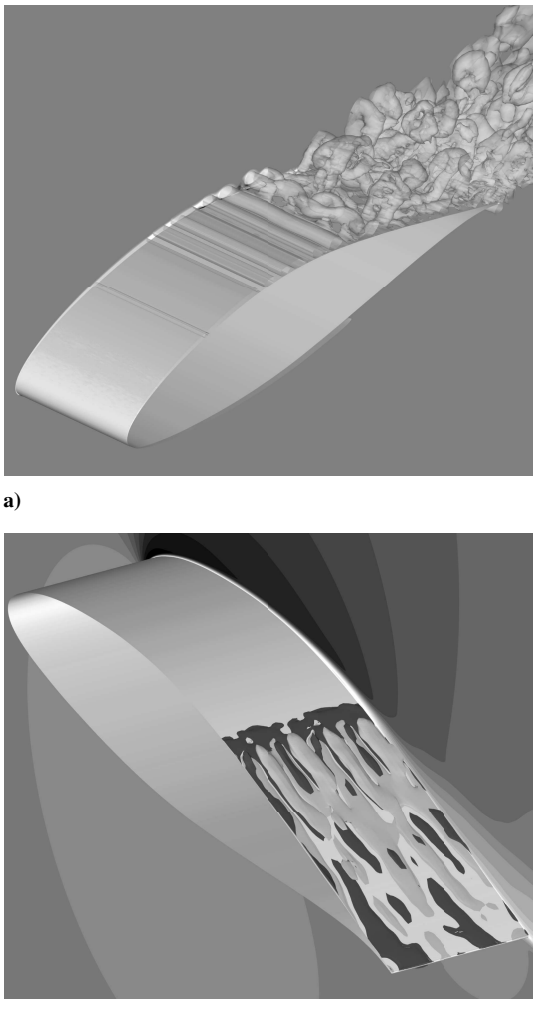

a) b)

Fig. 28 Images of a) instantaneous isocontours of spanwise vorticity ($-100 < \omega_z < 100$) and isosurfaces of $Q = 1$ and b) isocontours of velocity magnitude and isosurfaces of $\omega_x = -10$, 10 for temporal average.

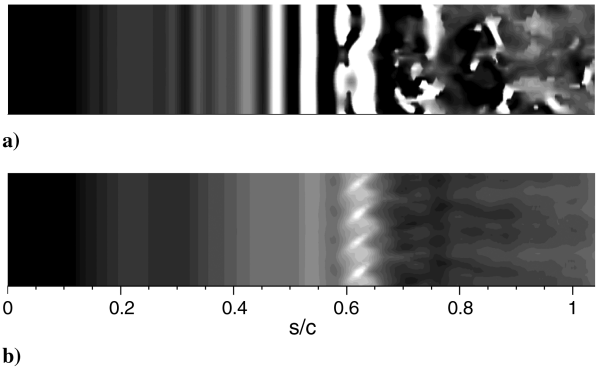

Fig. 29 Images of a) instantaneous and b) time-averaged suction-side skin-friction coefficient ($-0.01 < c_f < 0.01$).

traces become more and more irregular, indicating transition to turbulence. (The spanwise disturbance wavelength is limited to the domain width of $0.2c$. This artificial limitation may result in an overemphasis of 2-D modes.) In the frequency domain (Fig. 25b) the 2-D modes associated with the actuation, $f = 5$ and $f = 10$, are seen to decay faster than for $B = 1$ (Fig. 19b), indicating that 2-D coherence is lost earlier. Mode amplitudes obtained from the simulation are shown in Fig. 26. Results from an LST were not included since the disturbance amplitudes shortly downstream of the VGJ holes were found to be too high (i.e., nonlinear) to allow for a comparison with linear theory. For $0.34 < s/c < 0.48$, the steady longitudinal vortex mode (0,1) is dominant. The mode is, however, dampened. Downstream of $s = 0.48$, all mode amplitudes have nonlinear amplitudes and few conclusions can be drawn other than that the flow is turbulent. When scrutinizing the time-dependent skin-friction coefficient, we noticed acoustic waves at the beginning and end of the jet pulse for $B = 1$ and 4. For $B = 4$, the pressure gradients associated with these waves were strong enough to induce local flow separation (Fig. 27). How these waves affect the transition process and the overall effectiveness of the flow control remains to be investigated in the future. We conclude that for $B = 4$ the dominant physical mechanisms are the generation of a pronounced steady streamwise vortex that promotes wall-normal mixing and an earlier transition of the flow, compared to the uncontrolled case. The control is not very efficient, as the streamwise vortex is not supported by the flow and dampened.

3. *Two-Dimensional Volume Forcing*

Finally, motivated by plasma actuators we also investigated 2-D volume forcing. Visualizations of the instantaneous and time-averaged flow are shown in Fig. 28. Similar to the uncontrolled flow (Fig. 8a), the laminar boundary layer is seen to first roll up into spanwise vortical structures before the flow transitions to turbulence. However, the spanwise structures are spaced more closely (the forcing frequency was $f = 5$, while the frequencies associated with the spanwise structures for the uncontrolled flow were $f \leq 1$) and persist longer. Compared to the flow control with pulsed VGJs (Figs. 17 and 23), the flow is seen to transition later. In the meantime, counter-rotating streamwise vortices (eight vortices, $\lambda_z = 0.05c$) and

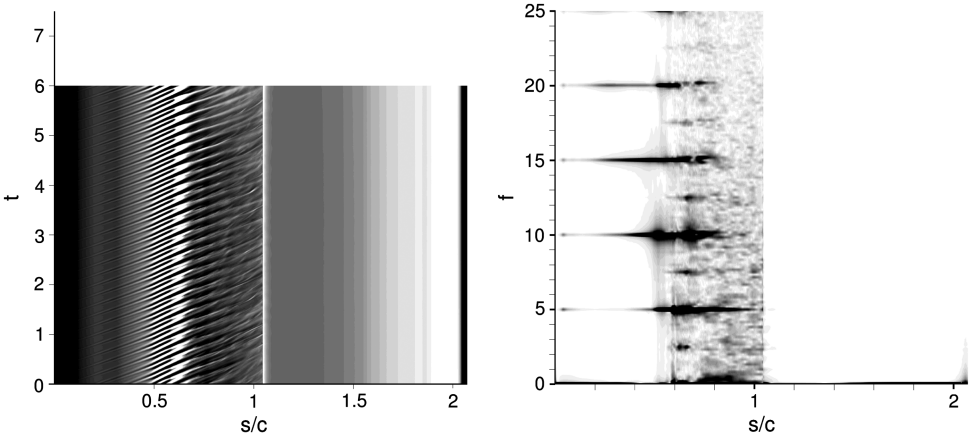

Fig. 30 Plots of a) time history of spanwise average of skin-friction coefficient ($-0.01 < c_f < 0.01$) and b) Fourier transform in time of skin-friction coefficient for spanwise mode $k = 0$ ($0 < A(c_f) < 0.001$).

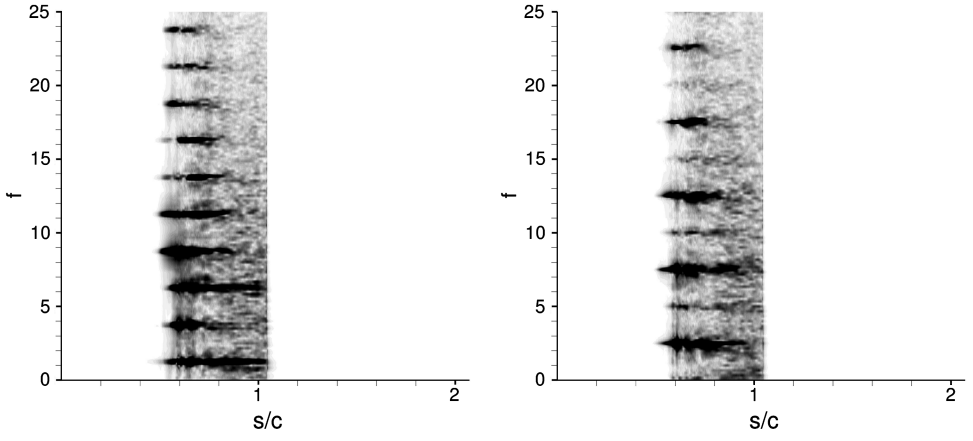

Fig. 31 Fourier transform in time of skin-friction coefficient for spanwise mode a) $k = 1$, and b) $k = 2$ ($0 < A(c_f) < 0.001$).

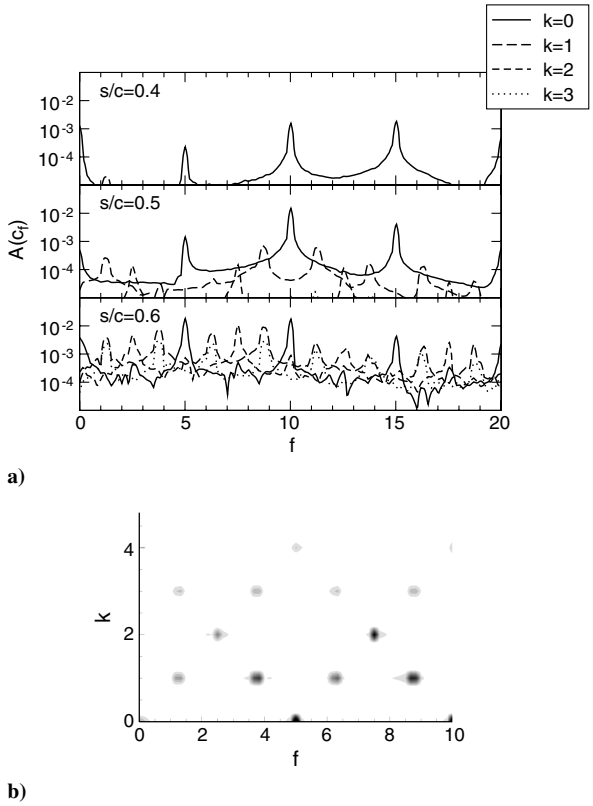

Fig. 32 Skin-friction coefficient disturbance amplitude spectra at a) three different downstream locations and b) $s/c = 0.6$ ($0 < A(c_f) < 0.01$).

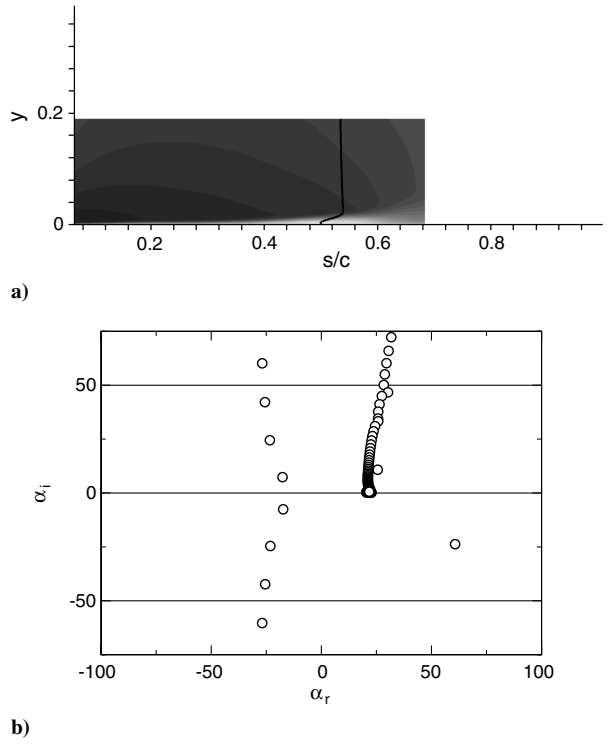

Fig. 33 Plots of a) isocontours of wall tangential velocity ($-0.3 < u < 2$) and velocity profile at $s/c = 0.503$ ($\Delta(s/c) = 0.025u$) and b) LST eigenvalue spectrum for $f = 5$ ($s/c = 0.503$).

a pronounced spanwise modulation of the skin-friction coefficient isocontour lines are seen near the reattachment location, hinting at the presence of a secondary instability mechanism (Figs. 28b and 29b). This observation is consistent with airfoil simulations by Jones et al. [7], who suggested that the 2-D vortex shedding makes the flow absolutely unstable to 3-D perturbations. The time–space diagram of the spanwise average of the skin-friction coefficient (Fig. 30a) shows very pronounced traces that extend all the way to the trailing edge ($s/c = 1.046$). Near $s/c = 0.5$, the spacing is $\Delta t = 0.1$ (half the period of the actuation). Downstream of $s/c = 0.6$, disturbances with $\Delta t = 0.2$ are dominant. In the frequency domain (Fig. 30b), strong disturbance amplification is observed for $f = 5$, 10, and 15, while the magnitude of disturbances with other frequencies is reduced, compared to the uncontrolled flow (Fig. 9a) and the cases with pulsed VGJs (Figs. 19b and 25b), indicating that the flow is transitioning later and less turbulent. Disturbance frequency spectra for the first two spanwise modes, $k = 1$ and $k = 2$, are shown in Fig. 31. For $k = 1$, maxima are seen near $f = 1.25 + 2.5n$ ($n = 0, 1, \ldots$), while for $k = 2$, maxima are seen near $f = 2.5 + 5n$ ($n = 0, 1, \ldots$). In Fig. 32a skin-friction coefficient disturbance amplitude spectra are shown for three different downstream locations. At $s/c = 0.4$, the 2-D modes ($k = 0$) are dominant, with peaks in the spectrum at $f = 5n$. At $s/c = 0.5$, disturbances with $f = 10 \pm 1.25$ and $k = 1$ appear. At $s/c = 0.6$, peaks are seen at $f = 1.25 + 2.5n$ for $k = 1$ and $f = 2.5 + 5n$ for $k = 2$. The mode diagram in Fig. 32b shares some similarities with mode diagrams that are typical for subharmonic breakdown scenarios (e.g., Kachanov and Levchenko [22]).

We also carried out an LST analysis. The time-averaged flow and a typical velocity profile as well as an eigenvalue spectrum obtained from the LST for $f = 5$ are shown in Fig. 33. The eigenfunction associated with the unstable mode in Fig. 33b is plotted in Fig. 34a. The stability diagram (Fig. 34b) is similar to the stability diagram for pulsed VGJs with $B = 1$ (Fig. 21b), indicating that linear (exponential) rather than transient growth is again the dominant

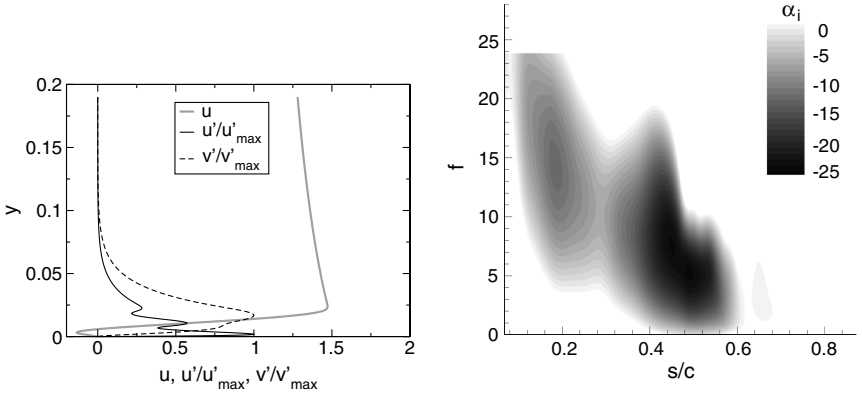

Fig. 34 Plots of a) velocity profile at $s/c = 0.503$ and normalized u and v components of eigenfunction for $\alpha = 60.7 - 23.7i$ and $f = 4.67$ and b) stability diagram.

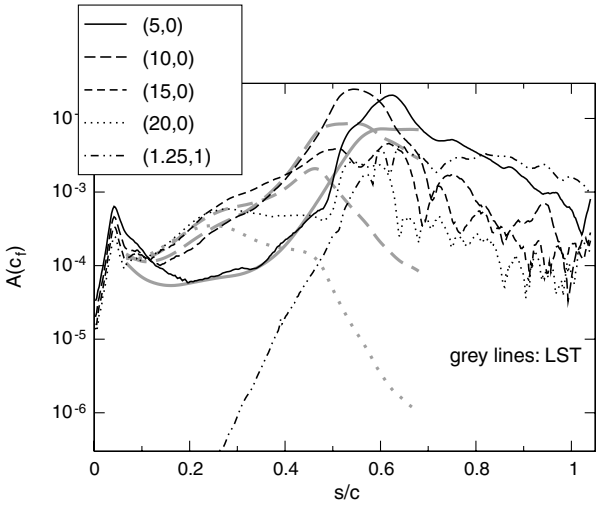

Fig. 35 Mode amplitudes obtained from DNS and LST.

mechanism. Figure 35 provides a comparison of mode amplitudes obtained from simulation and LST. Up to $s/c = 0.81$ the 2-D modes are dominant. The frequency of the dominant 2-D mode is progressively reduced in the downstream direction, starting from $f = 20$ for $0.11 < s/c < 0.23$ to $f = 15$ for $0.23 < s/c < 0.41$ and $f = 10$ for $0.41 < s/c < 0.60$ to, finally, $f = 5$ for $0.60 < s/c < 0.81$. This observation is consistent with the stability diagram (Fig. 34b), which shows larger growth rates for the higher frequencies in the upstream region. The disturbance amplitudes of the 2-D modes closely follow the LST prediction, indicating that a linear instability is responsible for the observed amplification of the 2-D modes. For $s/c > 0.48$, mode (10,0) grows faster than predicted by LST and reaches saturation near $s/c = 0.54$. Near $s/c = 0.5$, mode (5,0) also deviates from the LST prediction. This stronger than linear growth may be the consequence of a resonance with mode (10,0). Compared to the uncontrolled flow and the cases with VGJ flow control, the 3-D disturbance amplitudes for $s/c < 0.4$ are much reduced. Based on these observations and earlier investigations of AFC for a LPT blade by harmonic blowing and suction through a slot [9], we conclude that the high effectiveness of the 2-D volume forcing is the result of a linear amplification of the disturbance input, which makes the control very efficient, and the presence of energetic 2-D spanwise structures (or rollers), which facilitate a strong wall-normal momentum exchange.

IV. Conclusions

When a geometrically scaled model of a full-size aircraft is built and flown, the airfoil chord Reynolds number is much smaller than for the full-size aircraft because of the smaller chord length and the lower airspeeds. At the low-Reynolds-number conditions, laminar separation can result in significant performance losses. We investigated separation control by pulsed angled vortex generator jets (VGJs) and two-dimensional (2-D) volume forcing (that was motivated by plasma actuators) for the NACA 64_3-618 airfoil at $Re = 64,200$ and $\alpha = 8.64°$. This Reynolds number is sufficiently low to allow for direct numerical simulations (no turbulence model). Pulsed angled VGJs with low blowing ratio ($B = 1$) were found to introduce 2-D disturbances that are amplified linearly (exponential disturbance growth) by the flow by a hydrodynamic instability mechanism. The disturbance amplification makes the control more efficient, as the energy required for the amplification is provided by the flow. Based on the present simulations and earlier research [9], we concluded that the primary control mechanism was the added wall-normal momentum exchange facilitated by the spanwise coherent structures. Based on this conclusion, we speculate that the control will likely become more effective if the initial 2-D disturbance amplitude is increased. This could be accomplished through wall-normal injection and/or through a reduction of the spanwise VGJ hole spacing. When the blowing ratio was raised to $B = 4$, the primary control mechanism changed. Similar to the approach of Hansen and Bons [21], the VGJ pitch angle in our simulation was 30° and a single-legged streamwise vortex was found to originate from the VGJ hole. The increased wall-normal mixing facilitated by this longitudinal vortex and the earlier transition of the flow compared to the uncontrolled flow appear to be the primary control mechanisms [8]. Different from the case with $B = 1$, the disturbance amplitudes downstream of the VGJ hole are already nonlinear, and hydrodynamic instability mechanisms of the flow are not exploited as effectively as for $B = 1$. The steady streamwise mode is dampened and the gain in lift is less than for $B = 1$. Overall, this leads to the conclusion that for the present application, VGJs are more efficient and effective when operated at lower blowing ratios. Finally, we also investigated flow control by 2-D volume forcing near the leading edge of the airfoil. A linear stability theory investigation showed that the disturbance input was amplified strongly by a hydrodynamic instability mechanism. In the upstream part, where the boundary layer is thinner, the higher frequencies experienced stronger amplification, while in the downstream part and in the separated shear layer, disturbances with lower frequencies experienced stronger amplification. The strong amplification of the disturbance input explains the high efficiency of the volume forcing when compared with the VGJ flow control. Because the disturbance input is purely 2-D, three-dimensional modes are suppressed and the resulting flow structures have strong spanwise coherence. Based on the present results and earlier research [9], we concluded that the added wall-normal momentum exchange facilitated by the spanwise coherent structures was the primary control mechanism.

Acknowledgments

This work was funded by the U.S. Air Force Office of Scientific Research under grant number FA 9550-05-1-0166, with John Schmisseur serving as Program Manager, and by NASA under grant number NNL07AA40C through a Small Business Technology Transfer program with Advanced Ceramics Research, Inc. High-performance-computing (HPC) resources were provided by the U.S. Department of Defense HPC Modernization Program.

References

[1] Gross, A., Pearman, C., Kremer, R., Napier, B., Gosla, C., Kurz, A., et al., "1/5 Scale Model of Aeromot 200S SuperXimango for Scaled Flight Research," AIAA Paper 2008-6416, Aug. 2008.

[2] Mack, S., Brehm, C., Heine, B., and Fasel, H., "Experimental Investigation of Separation and Separation Control of a Laminar Airfoil," AIAA Paper 2008-3766, June 2008.

[3] Heine, B., Mack, S., Kurz, A., Gross, A., and Fasel, H. F., "Aerodynamic Scaling of General Aviation Airfoil for Low Reynolds Number Application," AIAA Paper 2008-4410, June 2008.

[4] Gaster, M., "The Structure and Behavior of Laminar Separation Bubbles," AGARD CP 4, Neuilly-sur-Seine, France, 1966, pp. 819–854.

[5] Brehm, C., Mack, S., Gross, A., and Fasel, H., "Investigation of an Airfoil at Low Reynolds Number Conditions," AIAA Paper 2006-3765, June 2008.

[6] Hain, R., Kähler, C. J., and Radespiel, R., "Dynamics of Laminar Separation Bubbles at Low-Reynolds-Number Aerofoils," *Journal of Fluid Mechanics*, Vol. 630, 2009, pp. 129–153. doi:10.1017/S0022112009006661

[7] Jones, L. E., Sandberg, R. D., and Sandham, N. D., "Direct Numerical Simulations of Forced and Unforced Separation Bubbles on an Airfoil at Incidence," *Journal of Fluid Mechanics*, Vol. 602, 2008, pp. 175–207.

[8] Bons, J. P., Sondergaard, R., and Rivir, R. B., "Turbine Separation Control Using Pulsed Vortex Generator Jets," *Journal of Turbomachinery*, Vol. 123, No. 2, 2001, pp. 198–206. doi:10.1115/1.1350410

[9] Gross, A., Balzer, W., and Fasel, H. F., "Numerical Investigation of Low-Pressure Turbine Flow Control (Invited)," AIAA Paper 2008-4159, June 2008.

[10] Rizzetta, D. P., and Visbal, M. R., "Numerical Investigation of Plasma-Based Flow Control for a Transitional Highly-Loaded Low-Pressure Turbine," AIAA Paper 2007-938, Jan. 2007.

[11] Huang, J., Corke, T. C., and Thomas, F. O., "Plasma Actuators for Separation Control of Low-Pressure Turbine Blades," *AIAA Journal*, Vol. 44, No. 1, 2006, pp. 51–57. doi:10.2514/1.2903

[12] Huang, J., Corke, T. C., and Thomas, F. O., "Unsteady Plasma Actuators for Separation Control of Low-Pressure Turbine Blades," *AIAA Journal*, Vol. 44, No. 7, 2006, pp. 1477–1487. doi:10.2514/1.19243

[13] Gaitonde, D. V., Visbal, M. R., and Roy, S., "Control of Flow Past a Wing Section with Plasma-Based Body Forces," AIAA Paper 2005-5302, 2005.

[14] Visbal, M. R., Gaitonde, D. V., and Roy, S., "Control of Transitional and Turbulent Flows Using Plasma-Based Actuators," AIAA Paper 2006-3230, 2006.

[15] Gross, A., and Fasel, H., "High-Order WENO Schemes Based on the Roe Approximate Riemann Solver," AIAA Paper 2002-2735, June 2002.

[16] Gross, A., and Fasel, H. F., "High-Order-Accurate Numerical Method for Complex Flows," *AIAA Journal*, Vol. 46, No. 1, 2008, pp. 204–214. doi:10.2514/1.22742

[17] Gross, A., and Fasel, H. F., "Multi-Block Poisson Grid Generator for Cascade Simulations," *Mathematics and Computers in Simulation*, Vol. 79, No. 3, Dec. 2008, pp. 416–428. doi:10.1016/j.matcom.2008.01.042.

[18] Rizzetta, D. P., and Visbal, M. R., "Numerical Investigation of Transitional Flow Through a Low-Pressure Turbine Cascade," AIAA Paper 2003-3587, June 2003.

[19] Gross, A., and Fasel, H. F., "Characteristic Ghost-Cell Boundary Condition," *AIAA Journal*, Vol. 45, No. 1, 2007, pp. 302–306. doi:10.2514/1.23130

[20] Hunt, J. C. R., Wray, A. A., and Moin, P., "Eddies, Stream, and Convergence Zones in Turbulent Flows," Center for Turbulence Research, Rept. CTR-S88, Stanford, CA, 1988.

[21] Hansen, L., and Bons, J., "Flow Measurements of Vortex Generator Jets in Separating Boundary Layer," *Journal of Propulsion and Power*, Vol. 22, No. 3, 2006, pp. 558–566. doi:10.2514/1.13820

[22] Kachanov, Y. S., and Levchenko, V. Y., "The Resonant Interaction of Disturbances at Laminar-Turbulent Transition in a Boundary Layer," *Journal of Fluid Mechanics*, Vol. 138, 1984, pp. 209–247. doi:10.1017/S0022112084000100

M. Visbal
Associate Editor